A Wide Load-Range and Compact MHz Wireless Power Transfer System based on Novel Reactance Compression Design and Edge Inductor

Huan Zhang, *Student Member, IEEE,* Yaoxia Shao, *Student Member, IEEE,* Ming Liu*, *Senior Member, IEEE,* Chengbin Ma, *Senior Member, IEEE*

Abstract—In MHz WPT systems, a varying reflected reactance due to a changing final load deteriorates the overall system performance, such as efficiency and output voltage stability. This paper aims to achieve a compact and robust MHz WPT system working over a wide range of load. A novel concept of reactance compression design is proposed to compress the variation of the reflected reactance through positioning of a "reactance window". Efficient receiving-side parameter design procedures are then developed to best compress the reactance variation and satisfy maximum output power requirement in a wide load range but without adding any other hardware. This makes it possible to directly apply the existing voltage source design using a modified Class E PA and current source design using LCC transformation network. An edge inductor also becomes worthy to replace the bulky air-core infinite inductor required by the modified Class E PA, thereby further improving circuit compactness. Finally, the receiving-side design concept and edge inductor were experimentally implemented to verify their performance over a 5–50 Ω load and with 20 W maximum final output power. The results well validate the improved reactance compression, output voltage stability, efficiency and harmonic distortions over the wide load range.

Index Terms—Edge inductor, load variation, megahertz, reactance compression, wireless power transfer (WPT).

I. Introduction

Wireless power transfer (WPT) systems operating at several MHz are now being expected to be a promising technology for the mid-range transfer of a medium amount of power. Generally, higher operating frequencies help improve the compactness and spatial freedom of the power transfer [1], [2]. The Class E topologies have been widely used in MHz WPT systems (including the power amplifiers (PAs) and rectifiers), because of their single-ended gate driving, zero-voltage

H. Zhang, Y. Shao, and C. Ma are with University of Michigan-Shanghai Jiaotong University Joint Institute, Shanghai Jiao Tong University, 800 Dongchuan Road, Minhang, Shanghai 200240, China (e-mail: hzhang_93@sjtu.edu.cn; yaoxiashao@sjtu.edu.cn; chbma@sjtu.edu.cn); M. Liu is with the Key Laboratory of Control of Power Transmission and Conversion of Ministry of Education, and the School of Electronic Information and Electrical Engineering, Shanghai Jiao Tong University, Shanghai 200240, China (e-mail: mingliu@sjtu.edu.cn).

switching (ZVS) operation and zero-voltage-derivation switching (ZVDS) operation. These advantages simplify the circuit configuration and improve efficiency [3]–[6]. Meanwhile, the traditional Class E PA does not perform as a current source or voltage source, and its performance is highly sensitive to the loading condition. This poses challenges for actual scenarios when the final load changes over a wide range. A modified design using a finite input inductor has been discussed to enable the Class E PA to maintain the ZVS operation and voltage source feature over a wide resistive load range [7], [8]. Note that as discussed later, in the MHz WPT systems, an obvious variation in the PA's reactive load is also possible, which may adversely affect the operation of the modified Class E PA.
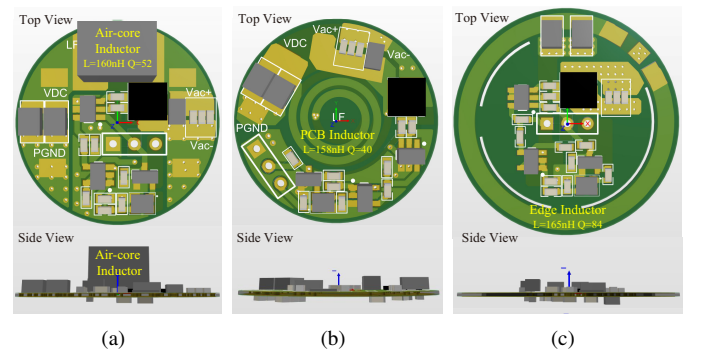

Fig. 1. PA with a different ac inductor. (a) Air-core inductor. (b) PCB inductor. (c) Proposed edge inductor.

At present, a bulky air-core inductor is usually used as the finite inductor in the modified Class E PA. Fig. 1(a) shows the layout of a modified Class E PA using a commercial air-core inductor. This type of inductor is especially large in height, which is unfavorable for a high PA power density. The PCB inductor can be employed to replace the bulky air-core inductor to decrease the height of the PA circuit board, as shown in Fig. 1(b). Due to the proximity effect, the quality factor of the PCB inductor is lower than that of the air-core inductor, especially when a relatively large inductance is required over a limited PCB space. In order to improve the quality factor and compactness at the same time, this paper proposes and implements a novel edge inductor design for the modified Class E PA. Fig. 1(c) shows the layout of a modified Class E PA using the edge inductor, where the inductor trace is along the PCB edge. This edge inductor makes full use of the

board space to enlarge the diameter and width of the inductor trace, namely achieving the same inductance with less turns and a higher quality factor.

In addition, in MHz WPT systems, the input impedance of the rectifier is no longer pure resistive [9]. It detunes the resonance of the receiving coil and leads to a reflected reactance on the transmitting side. With an ideal fixed final load, the rectifier input reactance can be fully compensated by the compensation capacitor of the receiving coil [10]. However, in real applications, the final load usually changes over time, which causes the varying reflected impedance seen on the transmitting side [9], [11]. This varying impedance, especially the varying reactance, will significantly impact the soft-switching and voltage / current-source operations of the most single-ended PAs, such as the Class E PA, Class EF_2 PA, and also the modified Class E PA using the finite inductor. To compensate the varying reactance, switch-capacitor array has been usually applied to tune the PA output impedance and maintain PA's ZVS condition [12]. However, this solution increases circuit complexity, size and cost, requires additional hardware for sampling and control, and potentially reduces reliability. To compress the impedance variation, passive LC networks or rectifiers using the finite inductor have been adopted to achieve the load independent operation of the single-ended Class E PAs [8], [13]. But these additional LC networks or the finite inductor on receiving side enlarge the size and introduce additional losses on the receiving side. Note that the receiving side, usually inside a mobile device, has strict limitations on size, weight, and power loss.

In this paper, a novel receiving-side design concept is proposed to compress the variation of the reflected reactance based on the input impedance analysis of Class E family of rectifiers and positioning of a "reactance window". This re-actance variation can be most effectively compressed through the developed parameter design of the receiving side, namely without adding any additional hardware. Therefore, the MHz WPT system can always maintain the ZVS operation and stable final output voltage. This advantage makes it possible to directly apply the existing PA / compensation designs into the MHz WPT systems (e.g., a voltage source through the modified Class E PA and classical LCC voltage / current source transformation network), when there is a wide range of load variation [14]. Thanks to the simplicity of the enabled PA / compensation designs, it becomes worthy to replace the originally bulky finite inductor in the modified Class E PA with a well-design edge inductor to further improve compactness [see Fig. 1(c)]. By combining the proposed receiving-side design concept and edge inductor design, a compact and robust final MHz WPT system can be achieved over a wide load range.

II. IMPEDANCE VARIATION ANALYSIS

Fig. 2 shows the configuration of a typical MHz WPT system, which consists of a PA, a compensation network, a pair of coupling coils, and a rectifier. In the figure, Z_{net} is the input impedance of the compensation network, namely the output impedance of the PA $Z_{pa}(= Z_{net})$; Z_{coil} is the input impedance of the transmitting coil; Z_{rec} is the input impedance

of rectifier; L, C, and r with different subscripts (tx and rx) are the self inductances, compensation capacitances, and self resistances of the two coils, and k is the mutual inductance coefficient. The receiving side uses a series compensation, which is suitable for the current-driven circuits, such as the Class E family of rectifiers [15], [16].
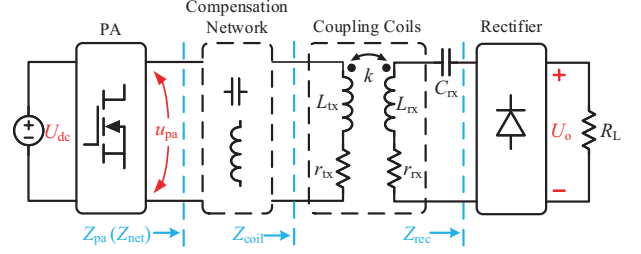

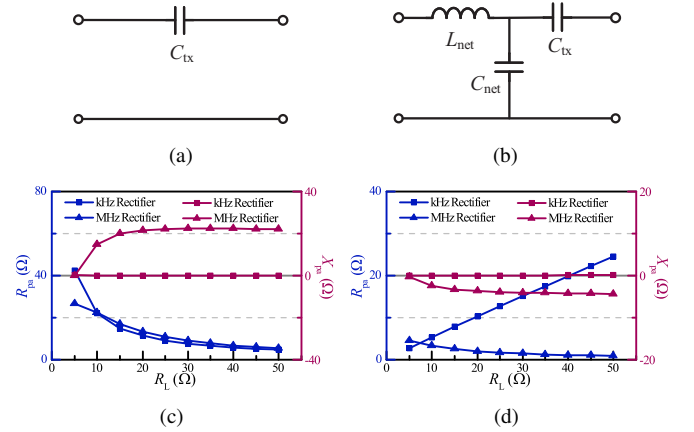Fig. 2. Configuration of a typical MHz WPT system.

Fig. 3. Impedance analysis. (a) Series compensation network. (b) LCC compensation network. (c) Z_{pa} of the primary series compensation network. (d) Z_{pa} of the primary LCC compensation network.

Fig. 3(a) and (b) show two popular compensation networks in conventional kHz WPT systems (i.e., series compensation and LCC compensation) that achieve constant-voltage or constant-current excitation with zero reactive power and soft switching [17]. Fig. 3(c) and (d) show different Z_{pa} when the WPT system operates at kHz or MHz, namely with a kHz rectifier or MHz rectifier. For comparison purposes, here the two rectifiers are both full-bridge ones. As shown in Fig. 3(c) and (d), the kHz system can always maintain a close-to-zero reactance X_{pa} even the final dc load R_L largely varies from 5 Ω to 50 Ω. In contrast, more complex impedance feature appears in the MHz system, which is caused by the large reflected reactance variation $|\Delta X_{ref}|$ [see the following Fig. 7]. Note that $|\Delta X_{ref}|$ is equal to $|\Delta X_{pa}|$ in Fig.3(c). As discussed in the following sections, this large $|\Delta X_{ref}|$ should be effectively compressed to provide a desirable working condition of the PA and compensation networks, such as through a novel design of the receiving side.

III. REFLECTED REACTANCE VARIATION COMPRESSION

The key of the proposed design is to make full use of the potential of the Class E family of rectifiers. Its purpose is to achieve reflected reactance variation compression but without adding any other components. The Class E family of rectifiers,
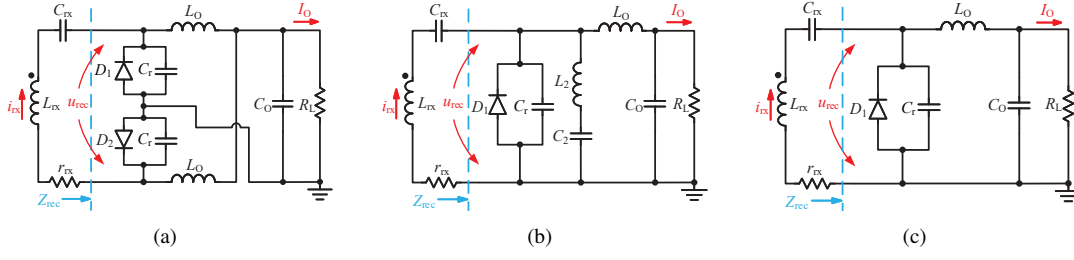
Fig. 4. Class E family of rectifiers. (a) Full-wave rectifier. (b) Class EF rectifier. (c) Half-wave rectifier.
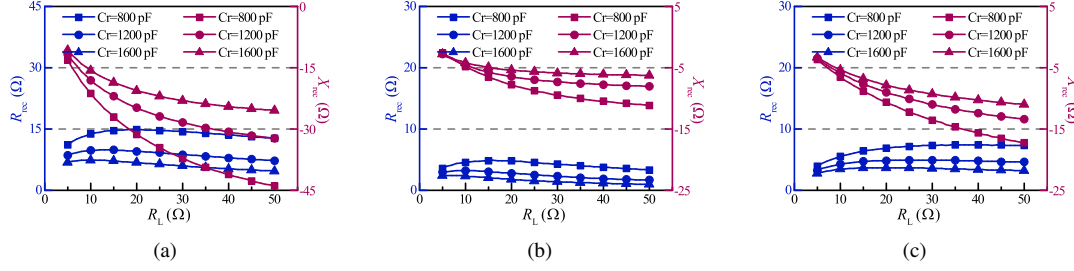

Fig. 5. Input impedances of Class E rectifiers versus R_{L}. (a) Full-wave. (b) Class EF. (c) Half-wave

such as the half-wave Class E, full-wave Class E and Class EF rectifier, are shown in Fig. 4. Those rectifiers have been widely used in MHz WPT systems mostly due to their high efficiency and low harmonic contents [18], [19]. In the figure, L_{O} is a choke inductor to block higher-frequency while passing dc current. The shunt capacitor C_{r} in this family of rectifiers also provides an additional degree of freedom to design the rectifier input impedance, Z_{rec} in the above Fig. 2.

A. Impedance Features of Class E Family of Rectifiers

Fig. 5 shows the input impedances of the Class E family of rectifiers with a varying R_{L}. The below variables are defined to describe the rectifier input impedance variation, including the reactance variation range $|\Delta X_{\mathrm{rec}}|$, resistance variation range $|\Delta R_{\mathrm{rec}}|$, and average resistance $\bar{R}_{\mathrm{rec}}$:

$$
\begin{aligned}
|\Delta X_{\mathrm{rec}}| &= |X_{\mathrm{rec,max}} - X_{\mathrm{rec,min}}|, \\
|\Delta R_{\mathrm{rec}}| &= |R_{\mathrm{rec,max}} - R_{\mathrm{rec,min}}|, \\
\bar{R}_{\mathrm{rec}} &= \frac{\int_{R_{\mathrm{L,min}}}^{R_{\mathrm{L,max}}} R_{\mathrm{rec}}\, dR_{\mathrm{L}}}{R_{\mathrm{L,max}} - R_{\mathrm{L,min}}}.
\end{aligned}
\tag{1}
$$

And the relationships of $|\Delta X_{\mathrm{rec}}|$ and $\bar{R}_{\mathrm{rec}}$ versus the diode shunt capacitor C_{r} are shown in Fig. 6.

Compared with the conventional full-bridge rectifier, the diode shunt capacitors C_{r} provide the Class E family of rectifiers with a unique ability to store and release energy. These resonant rectifiers can be equivalently represented by a simplified $R_{\mathrm{eq}}C_{\mathrm{eq}}$ parallel circuit. Thus, their input impedances can be straightforwardly expressed as:

$$
Z_{\mathrm{rec}} = \frac{R_{\mathrm{eq}}}{1 + \omega^2 C_{\mathrm{eq}}{}^2 R_{\mathrm{eq}}{}^2} - \mathrm{j}\frac{\omega C_{\mathrm{eq}} R_{\mathrm{eq}}{}^2}{1 + \omega^2 C_{\mathrm{eq}}{}^2 R_{\mathrm{eq}}{}^2} = R_{\mathrm{rec}} + \mathrm{j}X_{\mathrm{rec}},
\tag{2}
$$

in which ω is the operating frequency, and expressions of R_{eq} and C_{eq} are in Appendix. Based on Fig. 5, Fig. 6 and (2), the below impedance features of the Class E family of rectifiers are summarized as follows:

1) reactance variation is much larger than that in the resistance, i.e., $|\Delta X_{\mathrm{rec}}| \gg |\Delta R_{\mathrm{rec}}|$;

2) reactance X_{rec} decreases monotonically when the load R_L increases;

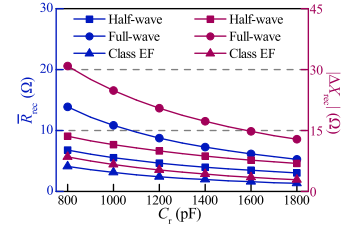3) $|\Delta X_{\mathrm{rec}}|$ and average resistance $\bar{R}_{\mathrm{rec}}$ decrease monotonically when C_{r} increases.

Fig. 6. $\bar{R}_{\mathrm{rec}}$ and $|\Delta X_{\mathrm{rec}}|$ versus diode shunt capacitor C_{r}.
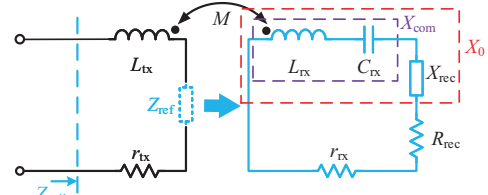

Fig. 7. Reflected impedance model.

B. Determination of Reactance Window Position

Fig. 7 shows the reflected impedance model of a WPT system, in which $Z_{\mathrm{ref}} = R_{\mathrm{ref}} + jX_{\mathrm{ref}}$ is the reflected impedance, representing the loading effect of the receiving side on the transmitting side. The resistance R_{ref} and reactance X_{ref} of Z_{ref} can be expressed as:

$$
R_{\mathrm{ref}} = \frac{(\omega M)^2 (R_{\mathrm{rec}} + r_{\mathrm{rx}})}{(R_{\mathrm{rec}} + r_{\mathrm{rx}})^2 + (X_{\mathrm{rec}} + X_{\mathrm{com}})^2},
\tag{3}
$$

$$
X_{\mathrm{ref}} = \frac{-(\omega M)^2 (X_{\mathrm{rec}} + X_{\mathrm{com}})}{(R_{\mathrm{rec}} + r_{\mathrm{rx}})^2 + (X_{\mathrm{rec}} + X_{\mathrm{com}})^2},
\tag{4}
$$

where $X_{\mathrm{com}} = \omega L_{\mathrm{rx}} - \frac{1}{\omega C_{\mathrm{rx}}}$ is a fixed compensation reactance, and M is the coupling coil mutual inductance ($= k\sqrt{L_{\mathrm{tx}}L_{\mathrm{rx}}}$). In the conventional design, X_{com} compensates the rectifier input reactance X_{rec} to achieve full resonance on the receiving

side [20]. However, this full resonance obviously cannot maintain within a wide load range. In Fig. 7, the total reactance of the receiving side X_0 is equal to:

$$X_0 = X_{\text{rec}} + X_{\text{com}} = X_{\text{rec}} + \omega L_{\text{rx}} - \frac{1}{\omega C_{\text{rx}}} \quad (5)$$

It decreases monotonically with an increasing load R_L, due to the fixed X_{com} and decreasing X_{rec} [see Fig. 5].
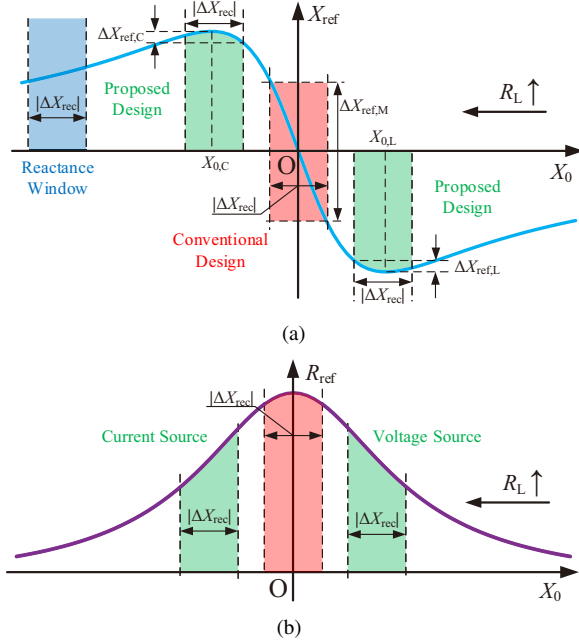

Fig. 8. Z_{ref} versus X_0. (a) Reactance X_{ref}. (b) Resistance R_{ref}.

From (3)–(5), a general relationship between the reflected impedance Z_{ref} and X_0 is summarized and shown in Fig. 8, assuming an almost constant R_{rec}. Note that from the above impedance feature (1), $|\Delta X_{\text{rec}}| \gg |\Delta R_{\text{rec}}|$. Here the blue line in Fig. 8(a) is the reflected reactance X_{ref}, and the purple line in Fig. 8(b) is the reflected resistance R_{ref}. With a fixed C_r and a specific load range, the range of the rectifier reactance variation $|\Delta X_{\text{rec}}|$ is also fixed, such as the blue "window" representing $|\Delta X_{\text{rec}}|$ in Fig. 8(a). Through this "window", the variation trend of the reflected impedance can be observed. Because the value of X_{com} changes with a different compensation capacitor C_{rx}, from (5), the "reactance window" shifts along the X_0 axis with different C_{rx}'s, as shown in the above two subfigures.

Again, in the conventional design, C_{rx} is simply tuned to fully compensate the rectifier reactance. Thus, the "reactance window" is in the red zone shown in Fig. 8(a). Unfortunately, this results in a sharp variation in the reflected reactance ($\Delta X_{\text{ref,M}}$) when R_L changes. As shown in the subfigure, the best reactance compression is achieved when the "reactance window" is located in the two green zones, in which X_{ref} smoothly changes around its peak value, namely a much smaller reactance variation [see $\Delta X_{\text{ref,C}}$ and $\Delta X_{\text{ref,L}}$ in Fig. 8(a)]. Therefore, the two design parameters on the receiving side, C_{rx} and C_r that decide the position of the "reactance window" and its width, should be accordingly determined to enable the best reactance compression performance. Note that moving the reactance window from the red zone to

the green zones may slightly sacrifice the coil efficiency (namely, deviation from the full resonance) and thus lead to a higher coil conduction loss. Meanwhile, as shown in the following experiments in Section VI, it significantly improves the PA efficiency under a wide load variation, which eventually contributes to a high system efficiency.

Based on (4) and $\frac{dX_{\text{ref}}}{dX_0} = 0$, the two peaks of the green zones, $X_{0,\text{C}}$ and $X_{0,\text{L}}$, can be derived as follows:

$$X_{0,\text{C}} = -\bar{R}_{\text{rec}} - r_{\text{rx}}, \quad (6)$$

$$X_{0,\text{L}} = \bar{R}_{\text{rec}} + r_{\text{rx}}, \quad (7)$$

which both relate to the resistances of the rectifier and receiving coil. Good reactance compression, namely small $\Delta X_{\text{ref,C}}$ and $\Delta X_{\text{ref,L}}$ in Fig. 8(a), can then be achieved by positioning the "reactance window" around the two peaks. As shown in Fig. 8(b), when the "reactance window" locates around the negative $X_{0,\text{C}}$, the receiving side works in a capacitive operation, and R_{ref} decreases monotonically with an increasing final load R_L. Considering the power conservation, the relationship between the final dc output voltage U_o and transmitting coil current I_{tx} is:

$$I_{\text{tx}}^2 R_{\text{ref}} = \frac{U_o^2}{R_L}. \quad (8)$$

Thus, a constant transmitting coil current is needed for a stable final dc output voltage, i.e., a current source.

On the other hand, when the "reactance window" locates around the positive $X_{0,\text{L}}$, the receiving side operates inductively, and R_{ref} increases monotonically with the increasing load R_L. Again, the relationship between the final dc output voltage U_o and PA output voltage amplitude across its load resistor $U_{\text{pa,R}}$ is as follows:

$$\frac{U_{\text{pa,R}}^2}{R_{\text{ref}}} = \frac{U_o^2}{R_L}. \quad (9)$$

This results in a close-to-proportional relationship between $U_{\text{pa,R}}$ and U_o, requiring a constant-voltage PA for a stable final dc output voltage, i.e., a voltage source.

IV. PARAMETER DESIGN ON RECEIVING SIDE

A. Determination of C_r and C_{rx}

Here, the reflected reactance compression is novelly achieved by designing C_r and C_{rx}, namely the receiving-side design but without adding any other components. From (5)–(7), C_{rx} can be theoretically calculated to guarantee that the middle of the "reactance window" always locates at $X_{0,\text{C}}$ or $X_{0,\text{L}}$. However, in actual scenarios, when R_L changes, the small variation in R_{rec}, which is assumed to be constant above (i.e., $|\Delta X_{\text{rec}}| \gg |\Delta R_{\text{rec}}|$), will slightly deform the X_{ref} curve in Fig. 8(a) [also refer to (4)]. Thus, the optimal "windows", i.e., the two green zones, in this subfigure needs to shift a bit for the best reactance compression, namely searching for the optimal C_{rx}.

Form Fig. 6 and Fig. 9(a), it can be seen that a higher C_r leads to a more sharply changing X_{ref} curve, a narrower "reactance window" and a larger ΔX_{ref}. On the other hand, Fig. 9(b) shows that a lower C_r corresponds to smaller R_{ref}'s,
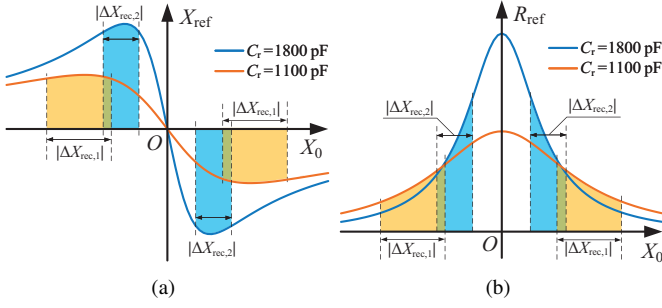
Fig. 9. Z_{ref} versus C_{r}. (a) Reactance X_{ref}. (b) Resistance R_{ref}.

which may influence the maximum output power. Therefore, in order to simultaneously 1) achieve a low reactance variation range and 2) meet the maximum output power requirement, the below efficient procedures in Fig. 10 are developed to obtain the optimal sets of C_{r} and C_{rx}, which is based on the analysis results in the above section. Note that the parameters of coupling coils (r_{rx}, r_{tx}, L_{rx}, L_{tx}), mutual inductance coefficient k, and final load variation range $R_{\text{L}} \in [R_{\text{L,min}}, R_{\text{L,max}}]$, are usually pre-determined in a target application.

The minimum C_{r} (i.e., $C_{\text{r,min}}$) should be first determined to guarantees the ZVS condition of the Class E family of rectifiers. From the above analysis such as through Fig. 8(a), it is known that, with a specific final load range, C_{r} corresponds to the "reactance window" width $|\Delta X_{\text{rec}}|$, and also determines the locations of the two peaks, $X_{0,\text{C}}$ and $X_{0,\text{L}}$. Then the above theoretically calculated C_{rx} is further fine tuned to achieve the best reactance compression. This greatly reduces the effort in a random search of C_{rx}. Therefore, the relationships between $|\Delta X_{\text{ref}}|$ and $R_{\text{ref,min}}$ can be quickly plotted under different C_{r}'s, such as shown in Fig. 11(a) for the inductive operation. The optimal C_{rx} lies on the dashed curve in the subfigure, along which each $R_{\text{ref,min}}$ corresponds to the smallest $|\Delta X_{\text{ref}}|$. The dashed optimal curve for the capacitive operation can be similarly obtained, as shown in Fig. 11(b).

The optimal curves in Fig. 11 show the results of the parameter design optimization, taking the constant parameters of coupling coils in Table I and a full-wave Class E rectifier as an example. In Fig. 11, each point of the optimal curves uniquely corresponds to a set of design parameters (i.e., C_{r} and C_{rx}). As discussed above, when the receiving side is tuned into the inductive operation, the PA should provide a constant voltage $U_{\text{pa,R}}$. Therefore, $R_{\text{ref,min}}$ in Fig. 11(a) determines the maximum final dc output power. Then, C_{r} and C_{rx} can be determined to meet the power requirement and locate over the optimal curve in Fig. 11(a). Similarly, when the receiving side is tuned into the capacitive operation, a constant transmitting coil current (I_{tx}) is required, which can be achieved by the LCC compensation network. Again, the optimal curve in Fig. 11(b) can guide to determine C_{r} and C_{rx} based on the power requirement.

TABLE I
EXAMPLE PARAMETERS OF COUPLING COILS.

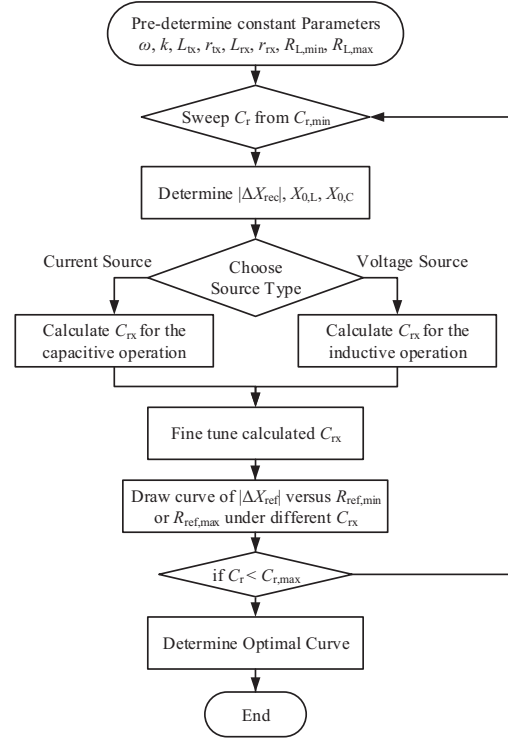| Fre [MHz]	L_{tx} [μH]	r_{tx} [Ω]	L_{rx} [μH]	r_{rx} [Ω]	k -	$R_{\text{L,min}}$ [Ω]	$R_{\text{L,max}}$ [Ω]
6.78	1.38	0.3	1.38	0.3	0.23	5	50

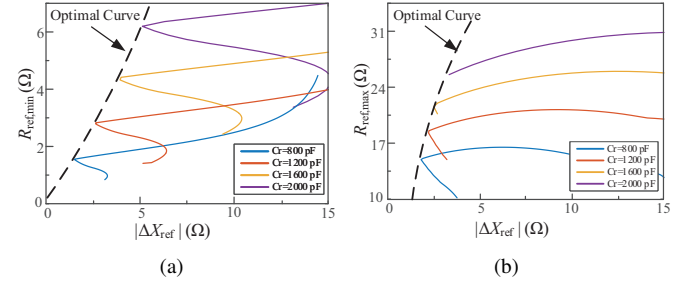Fig. 10. An efficient procedure to obtain the optimal sets of C_{r} and C_{rx}.

Fig. 11. The results of the parameter design optimization. (a) $R_{\text{ref,min}}$ and $|\Delta X_{\text{ref}}|$ in the inductive operation. (b) $R_{\text{ref,max}}$ and $|\Delta X_{\text{ref}}|$ in the capacitive operation.

B. PA and Compensation Design

As mentioned above, $|\Delta X_{\text{ref}}|$ can be effectively compressed based on the proposed design of the receiving side (i.e., C_{r} and C_{rx}). This makes it possible to directly apply the existing PA and compensation network design into wide load-range MHz WPT systems, such as systems with the modified Class E PA using a finite inductor and classical LCC compensation network.
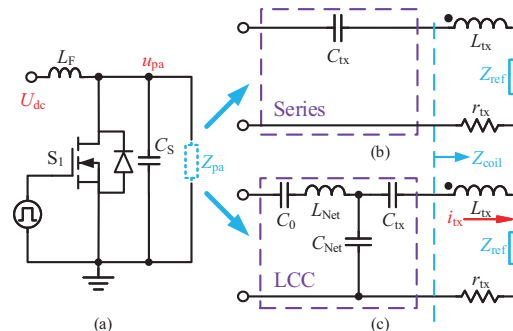

Fig. 12. PA with different compensation networks. (a) Modified Class E PA using a finite inductor. (b) Series compensation network. (c) LCC compensation network.

1) Voltage Source Design: As shown in Fig. 12(a), the modified Class E PA, which uses a finite inductor L_F, can provide a constant output voltage over a wide range of the PA resistive load due to the resonance between L_F and the switch parallel capacitor C_S. Thus, the PA can work as a voltage source when combined with a series compensation network [see Fig. 12(b)]. Meanwhile, this PA is also known to be sensitive to the load reactance variation and small load resistance [7]. However, thanks to the above proposed reactance compression, the PA parameters can be straightforwardly determined, such as described in [7], [8]. With a specific input dc voltage U_{dc} and required maximum PA output power $P_{pa,max}$, the minimum PA load can be calculated as:

$$R_{pa,min} = \frac{(1.58U_{dc})^2}{2P_{pa,max}} = R_{ref,min} + r_{tx}. \qquad (10)$$

Based on the value of $R_{ref,min}$=$(R_{pa,min} - r_{rx})$ calculated in (10) and the optimal curve in Fig.11(a), the parameters of the receiving side, C_r and C_{rx}, can be determined. The PA parameters, L_F and C_S, can also be calculated according to $R_{pa,min}$ [7]. Then C_{tx} can be accordingly designed using (11), in which X_{ref} corresponds to the minimum dc load (i.e., the maximum output power) [8]:

$$j\omega L_{tx} + \frac{1}{j\omega C_{tx}} + jX_{ref} \approx j0.2663\omega L_F. \qquad (11)$$

2) Current Source Design: The LCC compensation network in Fig. 12(c) can be used to transform a voltage source into a current source under a varying load resistance [14]. However, the current source operation can not be guaranteed when there is a large variation in the reflected reactance X_{ref}. Again, through the proposed reactance compression, the classical LCC network can fully achieve its design target, i.e., enabling a current source. The characteristic impedance of the LCC network X_{LCC} is [14]:

$$X_{LCC} = \sqrt{(r_{tx} + R_{ref,max}) R_{pa,min}} = \frac{1}{\omega C_{Net}}. \qquad (12)$$

In order to achieve the smallest possible $|\Delta X_{ref}|$, C_r needs to be small and at the same time guarantee the ZVS operation of the full-wave Class E rectifier over the target load range; Then, from the optimal curve in Fig. 11(b), the corresponding C_{rx} and $R_{ref,max}$ can be determined to calculate the LCC network's characteristic impedance in (12). Then C_{tx} can be designed based on (13),

$$X_{LCC} = X_{ref} + \omega L_{tx} - \frac{1}{\omega C_{tx}}. \qquad (13)$$

V. DESIGN OF EDGE INDUCTOR

A. Optimal Design

The above proposed receiving-side design concept provides effective compression of the reflected reactance variation. It enables a straightforward application of the existing modified Class E PA. Meanwhile, as explained in the introduction, unlike the traditional Class E PAs using infinite inductors, the modified Class E PAs in Fig. 12(a) employ a finite inductor. In practice, separate bulky finite inductors in the PAs greatly enlarge the size, especially in the height. Thanks to

the simplicity of the above PA and compensation designs, an novel edge inductor becomes worthy to implement a high-performance inductor and achieve compactness. As shown in Fig. 13, d is the trace width of the edge inductor; D_{out} and D_{in} are the outer diameter and inner diameter, and $D_{in,min}$ is determined by the PCB layout. The existing formula for the design of planar spiral inductor can be used to estimate the required size and shape of the PCB according to a target inductance L_F [21]:

$$L = \frac{\mu_0 N^2 D_{avg} A_1}{2} \left[\ln\left(\frac{A_2}{\rho}\right) + A_3\rho + A_4\rho^2 \right], \qquad (14)$$

where μ_0 is the vacuum permeability; N is the turns of the spiral inductor in a single layer; ρ is the fill ratio that is defined as $\frac{D_{out} - D_{in}}{D_{out} + D_{in}}$; D_{avg} is the average diameter of the PCB trace (i.e., $\frac{D_{out} + D_{in}}{2}$); and A_i's $(i = 1, ..., 4)$ are the coefficients depending on the shape of the PCB winding.
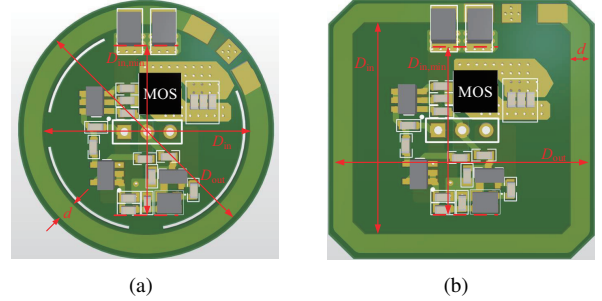

Fig. 13. PCB layout of the edge inductors. (a) Circular. (b) Square.

In order to further enhance the compactness, both the top and bottom layers are utilized for the winding. In a double-layer PCB design, the edge inductor is equivalent to a cascade of two windings, and its total inductance is:

$$L_{total} = L_{top} + L_{bottom} + 2M_{edge}, \qquad (15)$$

where L_{top} and L_{bottom} are the inductances of the top and bottom windings. They can be calculated by (14). And M_{edge} is the overall mutual inductance between the top and bottom windings. It can be obtained by summing the partial mutual inductances between windings in the two layers [22]. The dc and ac resistances of the edge inductor are:

$$R_{dc} = \rho_c \frac{l_c}{d \cdot t_c}, R_{ac} = R_{dc} \frac{t_c}{\delta \left(1 - e^{-\frac{t_c}{\delta}}\right)}, \qquad (16)$$

where ρ_c is copper resistivity; l_c is the length of edge inductor including the top and bottom windings; t_c is the thickness of PCB copper layer; d is the width of inductor trace; δ is the skin depth that is equal to $\sqrt{2\rho_c/\mu_c\omega}$.

For 1) a high efficiency of the edge inductor and 2) compact circuit design, the below bi-objective optimization problem is

formulated:

OBJ1 : min R_{ac}

OBJ2 : min $V_{\text{edge}} = \begin{cases} \pi D_{\text{PCB}} \left(D_{\text{out}}^2 - D_{\text{in,min}}^2 \right) & \text{for Cir.} \\ D_{\text{PCB}} \left(D_{\text{out}}^2 - D_{\text{in,min}}^2 \right) & \text{for Squ.} \end{cases}$

s.t. $\dfrac{|L_{\text{total}} - L_F|}{L_F} \leq 3\%$

$D_{\text{out}} - 2d \geq D_{\text{in,min}}$

$D_{\text{out}} \leq D_{\text{out,max}}$

(17)

In the above optimization problem, the design variables are outer diameter D_{out}, trace width d, and winding turns N of both top and bottom layers. The first constraint defines the tolerance (3% here) for the deviation from the target inductance L_F (i.e., required inductance in the PA design); $D_{\text{in,min}}$ is determined by the components layout; and $D_{\text{out,max}}$ limits the area of the PA board.

TABLE II
DESIGN PARAMETERS OF AN EXAMPLE MODIFIED CLASS E PA.

U_{dc}	$P_{\text{pa,max}}$	$R_{\text{pa,min}}$	k_{f}	L_F
12 V	25 W	7.19 Ω	$1.3 \sim 1.5$	$160 \sim 190$ nH

Target design parameters of an example modified Class E PA are shown in Table II. Ratio k_{f} is defined to balance the resonance losses and load modulation range, and the target inductance L_F can then be determined [7]. Assuming $D_{\text{in,min}} = 21$ mm and $D_{\text{out,max}} = 30$ mm, the above optimization problem in (17) is solved by sweeping the design variables D_{out} and d and the results are shown in Fig. 14. In the present parameter setting, only $N = 1$ (one turn in each layer) has a feasible solution. It is interesting to note that the circular edge inductor has better performance (i.e., smaller R_{ac} under the same V_{edge} along its Pareto front) to implement a smaller inductance, while the square one is better for a larger inductance, as respectively shown in Fig. 14(a) and (b).
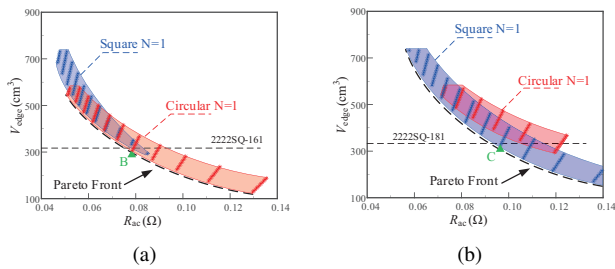

Fig. 14. Optimization of edge inductor. (a)$L_F = 170$ nH. (b)$L_F = 190$ nH.
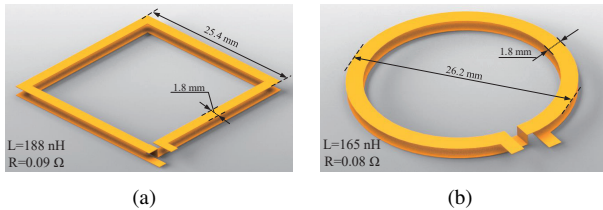

Fig. 15. Edge inductor models. (a) Square: $D_{\text{out}} = 25.4$ mm. (b) Circular: $D_{\text{out}} = 26.2$ mm.

The designs at B and C in Fig. 14 are chosen, whose inductances are equivalent to the widely-used commercial inductor 2222SQ-161 / 181 from Coilcraft [see Table III]. As shown in Fig. 15, design B corresponds to a circular edge inductor with

$D_{\text{out}} = 26.2$ mm, $d = 1.8$ mm and $L_{\text{total}} = 165$ nH, and design C is a square one with $D_{\text{out}} = 25.4$ mm, $d = 1.8$ mm and $L_{\text{total}} = 185$ nH.

TABLE III
MEASURED PARAMETERS OF INDUCTORS OPERATING AT 6.78 MHz.

Type	L [nH]	ESR [mΩ]	Q [-]	Height [mm]	Volume [mm^3]
Circular Edge Inductor	165	84	84	1.6	308
Square Edge Inductor	188	93	86	1.6	327
Coilcraft 2222SQ-161	160	130	52	6	318
Coilcraft 2222SQ-181	180	140	52	6	331

Table III lists the measurement results of the above two edge inductors and commercial Coilcraft inductors. It can be seen that the edge inductors can achieve a similar inductance, a higher quality factor, and significantly reduced height (73.3% reduction). These improvements not only enhance the compactness but also the efficiency of a final MHz WPT system.

B. Cross Coupling Analysis

Since the design of the edge inductor aims to achieve a compact PA, it always requires a small inductor both in size and inductance. As shown in Fig. 16(b), the mutual inductance between the edge inductor and transmitting coil (M_{c}) is also small, according to the simulation and test results. Even the edge inductor is very close to the transmitting coil (0 mm), the mutual inductance is only 15 nH. When the distance is greater than 1 cm, the mutual inductance rapidly drops to less than 6 nH. If the shielding measure in the following subsection is applied, M_{c} will be further reduced.
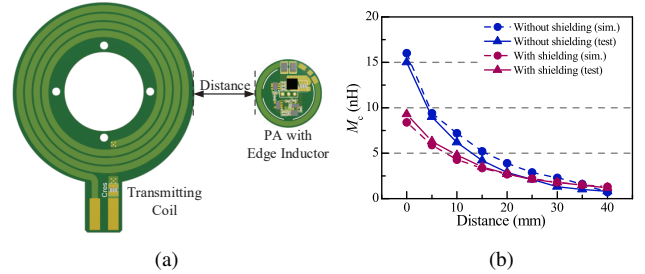

Fig. 16. Cross coupling analysis. (a) Schematics. (b) Mutual inductances between the edge inductor and transmitting coil ("sim.": simulation).

Assuming that the ac current in L_F is a triangle wave because of the small inductance and high frequency switch. This current lags the switch signal by 90 degrees and the amplitude of fundamental current in L_F is

$$I_{\text{dc1}} \approx -j \frac{4U_{\text{dc}}}{\pi \omega L_F}. \tag{18}$$

The induced voltage in the transmitting coil due to the cross coupling is

$$U_{\text{F,tx}} = j\omega M_{\text{c}} I_{\text{dc1}} \tag{19}$$

For the voltage-source design, based on the edge inductor's winding direction, the influence of the cross coupling on the transmitting coil current can be represented by the below current ratio [8]:

$$\text{R} = \frac{I'_{\text{tx}}}{I_{\text{tx}}} \approx \frac{1.58U_{\text{dc}} \pm U_{\text{F,tx}}}{1.58U_{\text{dc}}} \approx 1 \pm 0.8 \frac{M_{\text{c}}}{L_F}, \tag{20}$$

where I'_{tx} is the coil current with the cross coupling. From Fig.16(b), M_{c} is much smaller than L_{F}, which indicates a negligible current variation caused by the cross coupling.

For the current-source design, I_{tx} is close-to-constant and with the same/opposite phase of I_{dc1} due to the LCC compensation network. Therefore, the cross coupling causes a small reactance variation ΔX_{cross} and can be compensated by C_{tx}.

$$\Delta X_{\text{cross}} = \pm \frac{|U_{\text{F,tx}}|}{|I_{\text{tx}}|} \approx \pm \frac{\omega M_{\text{c}} I_{\text{dc1}}}{\frac{1.58 U_{\text{dc}}}{X_{\text{LCC}}}} \approx \pm 0.8 X_{\text{LCC}} \frac{M_{\text{c}}}{L_{\text{F}}} \quad (21)$$

C. Shielding Analysis

Practically, due to its planar structure, the use of the edge inductor may cause a more obvious electromagnetic interference (EMI) problem compared with the air-core inductor. Shielding measures can be utilized in EMI-sensitive applications. As shown in Fig. 17(c), the "magnetic coat" using flexible magnetic sheets (such as IBF15-180DD from TDK corporation) could effectively restrain the magnetic flux. Note that the "magnetic coat" increases the inductance. Thus, in order to achieve the similar inductance, the edge inductor in Fig. 17(c) only has one turn and its size is slightly larger.
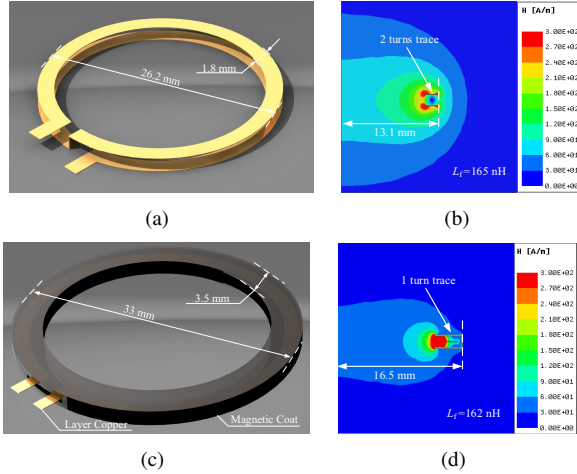

Fig. 17. Shielding measure. (a) Model without "magnetic coat" (two-turn inductor). (b) Magnetic field simulation without "magnetic coat" (two-turn inductor). (c) Model with "magnetic coat" (one-turn inductor). (d) Magnetic field simulation with "magnetic coat" (one-turn inductor).

The shielding also suppresses the inductance change of the edge inductor, which is particularly helpful when there is a metal case or heat sink nearby. As shown in Fig. 18(a) and (b), using the "magnetic coat", the inductance change is reduced by more than two-thirds under the same vertical distance (2 mm) of an aluminum plate. On the other hand, the modified Class E PA with a finite inductor (i.e., the edge inductor here) in Fig. 12 utilizes the resonance between L_{F} and C_{S} to achieve its ZVS operation. Based on [7], a smaller L_F still guarantees the ZVS operation [see Fig. 18(c)]. The actual environments could be certainly much more complex, which require comprehensive simulation to investigate and improve.

VI. Prototypes and Experiments

A compact 6.78 MHz WPT prototype with 20 W maximum output power is built to validate the proposed reactance compression and edge inductor design. And conventional design
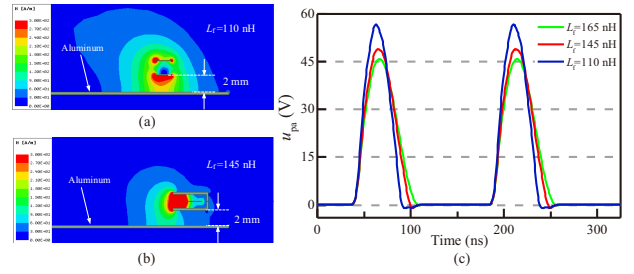

Fig. 18. Inductance changes under the same 2 mm vertical distance of an aluminum plate. (a) Magnetic field simulation without "magnetic coat". (b) Magnetic field simulation with "magnetic coat". (c) PA switch simulation waveforms ($C_{\text{S}} = 2000$ pF).
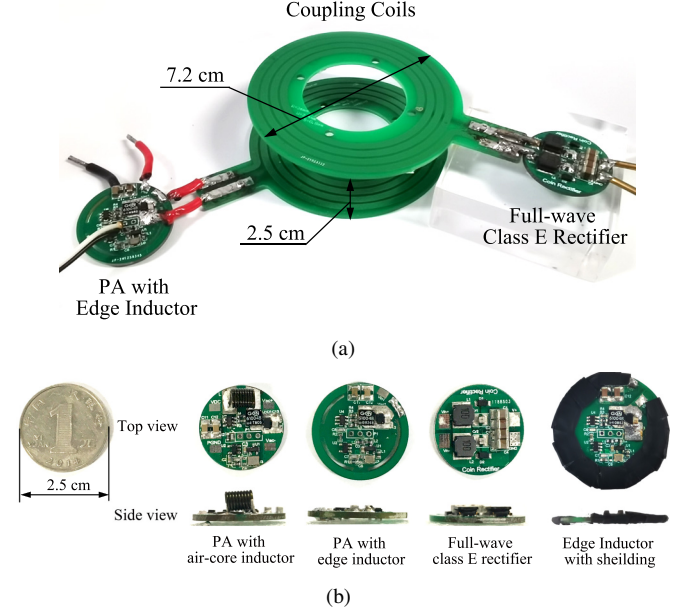

Fig. 19. Experimental system. (a) Setup. (b) PA sizes using the edge inductor and commercial air-core inductor.

of the is also applied for comparison purposes. The prototype system in Fig. 19(a) consists of a PA using the circular edge inductor, coupling coils and a circular full-wave Class E rectifier, namely a new compact "coin"-shaped WPT system. The diameters of the coupling coils are both 7.2 cm and transfer distance is 2.5 cm. In Fig. 19(b), the PCBs of the PA and rectifier have almost the same size with a coin (25 mm in diameter). Compared with the PA using the commercial air-core inductor 2222SQ-161, the PA using the edge inductor obviously decreases its height, namely improved compactness. DFLS240 is used as the rectifying diode. GaN MOSFET GS61004B is chosen as the PA switch, and is driven by LM5114BMF. It should be noted that the parasitic capacitors of the components are considered in the following parameter design.

A. Conventional Designs

In the following experiments, the conventional receiving side design is based on Ref. [18], in which the shunt capacitance C_{r} is chosen to achieve $D = 0.49$ duty cycle of rectifying diodes under the minimum dc load, i.e., $R_{\text{L}} = 5\ \Omega$ here. This enables the highest output power capability of the Class E rectifier. C_{rx} is then determined to fully compensate the rectifier input reactance under an intermediate dc load
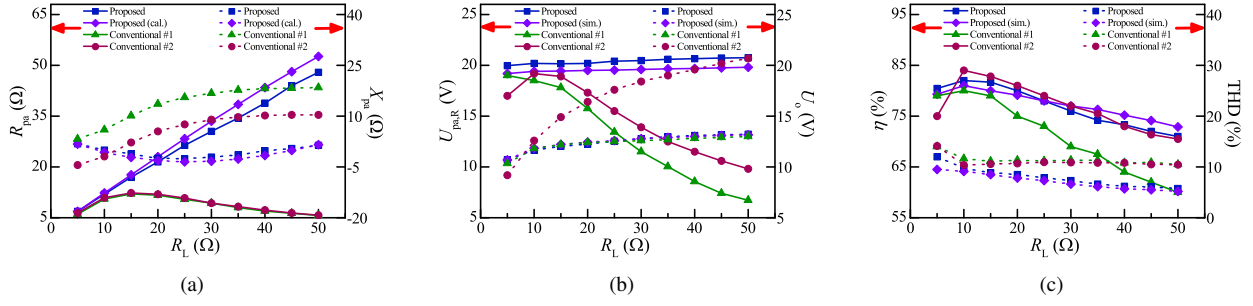
Fig. 20. Experimental results of the voltage-source prototype ("cal.": calculation; "sim.": simulation). (a) Z_{pa} vs R_L. (b) $U_{pa,R}$ and U_o vs R_L. (c) η and THD vs R_L.

(R_L=15 Ω) to improve the robustness of the final WPT system in a straightforward manner, when there are variations in the final load.

In the voltage-source prototype, C_{tx} can be designed based on either the minimum dc load or intermediate dc load, namely a different focus on the maximum output power or robustness. Thus, after determining C_r and C_{rx}, there are two possible designs of C_{tx} using (11):

- Conventional design #1: C_{tx} is determined when X_{ref} corresponds to the 5 Ω dc load.
- Conventional design #2: C_{tx} is determined when X_{ref} corresponds to the 15 Ω dc load.

As to the current-source prototype, due to the existence of the LCC compensation network, C_{tx} can be mainly designed to meet the requirement of maximum output power. Therefore,

- Conventional design #3: C_{tx} is determined to match X_{LCC} with the 5 Ω dc load [refer to (13)].

TABLE IV
DESIGN PARAMETERS OF VOLTAGE-SOURCE PROTOTYPE.

Design	C_r [pF]	C_{rx} [pF]	C_{tx} [pF]	L_F [nH]	C_S [pF]
Proposed Design	2100	616	510	165	1800
Conventional Design #1	800	763	472	165	1800
Conventional Design #2	800	763	423	165	1800

B. Voltage-source Prototype

The design parameters of the voltage-source prototype are listed in Table IV. In the proposed design, the shunt capacitance C_r and the compensation capacitor on the receiving side C_{rx} are determined from Fig. 11(a) with $R_{ref,min} = 7.1\Omega$ [refer to Table II]. Fig. 20(a) shows the results of the PA output impedances ($Z_{pa} = R_{pa} + jX_{pa}$). Thanks to the proposed reactance compression design, compared with the conventional design, the variation in the PA output reactance is compressed almost three times. The PA output resistance increases monotonically in an almost linear manner with an increasing R_L, when the receiving side is in the inductive operation. This characteristic is suitable for a voltage source that provides the maximum output power under the minimum dc load and maintains a relatively constant output voltage.

Furthermore, Fig. 20(b) compares the PA input voltage and final output voltage. Note $U_{pa,R}$ represents the voltage amplitude across the PA output resistance. With the proposed design, the final dc output voltage U_o only has 8% fluctuations
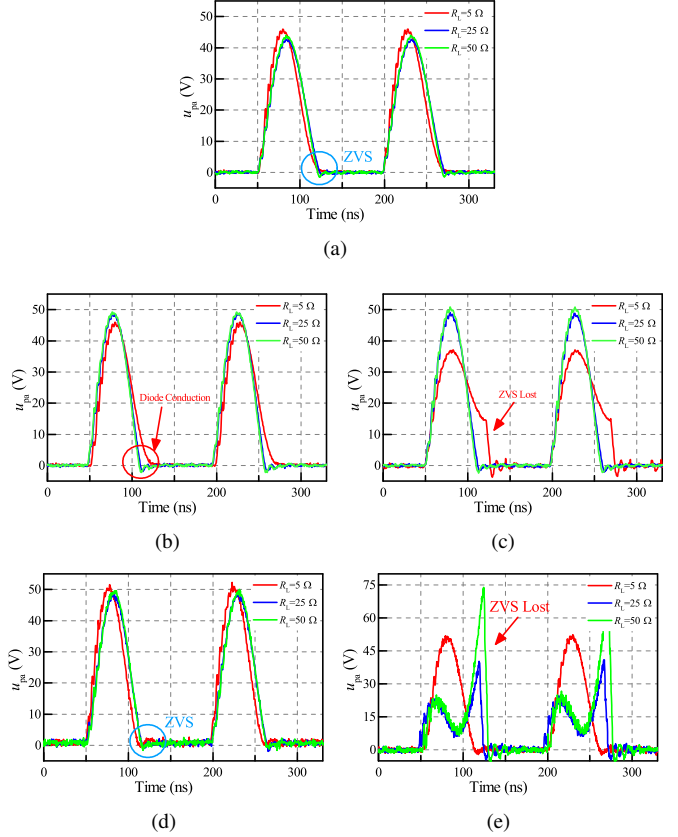

Fig. 21. PA drain-source voltage waveforms under 5, 25, and 50 Ω dc loads. (a) Proposed design for the voltage-source prototype. (b) Conventional design #1 for the voltage-source prototype. (c) Conventional design #2 for the voltage-source prototype. (d) Proposed design for the current-source prototype. (e) Conventional design #3 for the current-source prototype.

over a wide load range (5–50 Ω), but without any additional hardware and active control. This greatly improves the output voltage stability through a simple and compact circuit configuration. Thanks to the stable reactance, the PA can always maintain its ZVS operation and high efficiency in a wide range of final dc load, as shown in Fig. 21(a). In contrast, the PA through the conventional designs either increases the parallel diode conduction time or significantly deviates from the ZVS operation when R_L varies, as shown in Fig. 21(b)(c). Therefore, the proposed design enables high and stable system dc-dc efficiency η over a wide load range, considering all the losses from PA to rectifier [see Fig. 20(c)]. In addition, the larger shunt capacitor C_r leads to a smaller duty cycle of the rectifying diodes, which causes a lower THD compared with that in the conventional design [18].
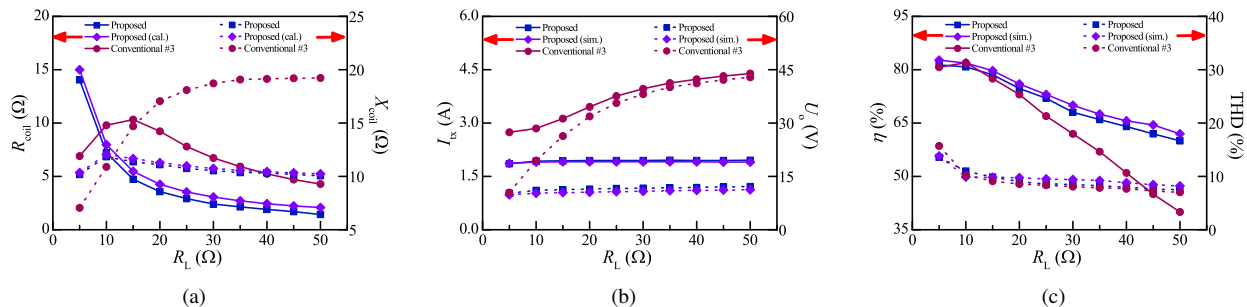
Fig. 22. Experimental results of the current-source prototype ("cal.": calculation; "sim.": simulation). (a) Z_{coil} vs R_{L}. (b) I_{tx} and U_{o} vs R_{L}. (c) η and THD vs R_{L}.

C. Current-source Prototype

As mentioned in Section IV-B2, a classical LCC network can be added to the modified Class E PA to enable constant current excitation of the transmitting coil. The PA parameters L_{F} and C_{S} are as same as the values in Table IV. And the receiving side should work in a capacitive operation. Because the LCC network provides additional design freedom, C_{r} can be directly chosen around 800 pF, as same as in the conventional design, to guarantee the 0.49 duty cycle of the rectifying diodes and minimum $|\Delta X_{\text{ref}}|$. Then, according to Fig. 11(b), $R_{\text{ref,max}}$ is equal to 15 Ω. And from (12), the required LCC network characteristic impedance X_{LCC} is 10.35 Ω. Other LCC network parameters can then be determined accordingly [14]. All the design parameters of the present prototype are listed in Table V.

TABLE V
DESIGN PARAMETERS OF CURRENT-SOURCE PROTOTYPE.

Design	C_{r} [pF]	C_{rx} [pF]	C_{tx} [pF]	L_{net} [nH]	C_0 [pF]	C_{net} [pF]
Proposed Design	800	468	435	307	22000	2200
Conventional Design #3	800	763	525	307	5700	3320

As shown in Fig. 22(a), compared with the conventional design #3, the compression of the reactance variation in X_{coil} is over six times thanks to the proposed design. The coil input resistance decreases monotonically with an increasing R_{L}, which is a preferred characteristic for a current source. As expected, over the entire load range, the amplitude of the current in the transmitting coil (I_{tx}) maintains almost constant around 1.9 A with less than 3% fluctuations, i.e., namely a current source [see Fig. 22(b)]. But the design procedures are much simpler than that in the existing work [8], [20]. The proposed design also enables a stable output dc voltage U_{o} with less than 8% fluctuations.

Similarly, the proposed current-source design always maintains the ZVS operation of the PA and thus a high system dc-dc efficiency η, as shown in Fig. 21(d) and Fig. 22(c). Meanwhile, the larger reflected reactance variation in conventional design leads to a smaller PA output resistance, which causes the hard switching in Fig. 21(e) and the low system efficiency. Note that because the rectifying diode shunt capacitor C_{r} in the both designs are the same, namely the almost same diode duty cycles, the two designs show similar THD [see Fig. 22(c)].
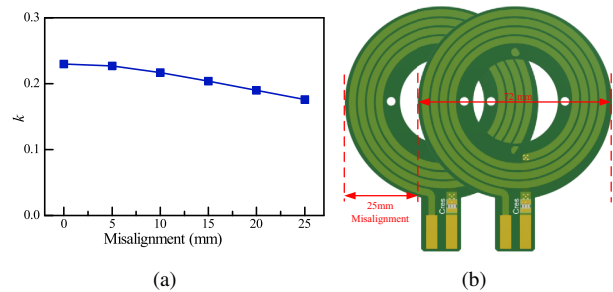

Fig. 23. Coupling coil misalignment. (a) k versus misalignment. (b) Coil schematic.

D. Coil Misalignment and No-load Condition

The MHz WPT is particularly known for its spatial freedom, i.e., improved transfer distance and robustness against coil misalignment. As shown in Fig. 23(a), the mutual inductance coefficient k is measured over a wide range of coil misalignment, 0–25 mm. Under the maximum 25 mm misalignment, more than one third of the coil diameter, k(=0.18) is largely reduced by 20%. According to (3)(4), this decrease of k compresses the impedance curves in Fig. 8 along y-axis by a fixed ratio, but the shapes of the curves still maintain. Fig. 24(a) shows the PA output impedance Z_{pa} when k changes from the original 0.23 (i.e., zero misalignment) to 0.18 (25 mm misalignment), taking the voltage-source prototype as an example. The PA drain-source voltage waveforms in Fig. 24(b) validate that the PA can still work properly under the large 25 mm coil misalignment.
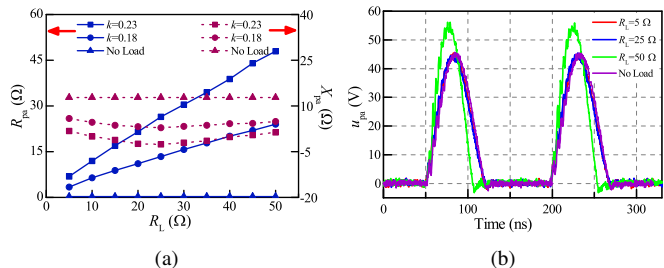

Fig. 24. Impedance variation and PA operation in the voltage-source prototype. (a) Comparison of PA output impedances. (b) PA drain-source voltage waveforms under $k = 0.18$.

In addition, a no-load condition is usually challenging for voltage sources. In the proposed voltage-source prototype, X_{ref} is negative and thus the series compensation network on the transmitting side needs to provide a positive reactance ($\omega L_{\text{tx}} - 1/\omega C_{\text{tx}} > 0$) [see Fig. 8(a)]. Thus, in the extreme condition of no load and maximum 25 mm coil misalignment,

this positive reactance still exists and continues to enable the ZVS operation of the modified Class E PA, as shown by the purple waveform in Fig. 24(b).

E. EMI Measurements

As shown in Fig. 25, a magnetic field probe and spectrum analyzer are used to conduct EMI measurement under the 20 W maximum output power. With the same distances (2, 4, 6 cm) between the edge inductor and the probe, the measured power spectrums in Fig. 25(b)(d) show obviously improved EMI performance through the shielding measure discussed in Section V-C.
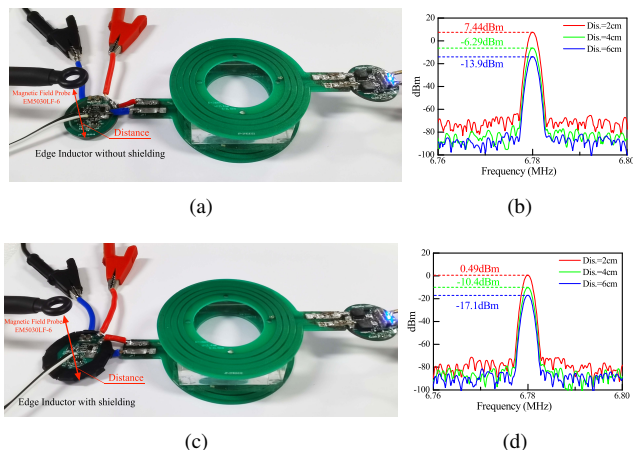

Fig. 25. EMI measurements. (a) Setup without shielding. (b) Power spectrum without shielding. (c) Setup with shielding. (d) Power spectrum with shielding.

The edge inductor may slightly impact the gate drive signal, as shown in Fig. 26. Attention should be paid to ensure the gate driver loop wiring as short as possible and use small footprint components. At the same time, as validated by the above experimental results, the modified Class E PA works properly when using the edge conductor. Note that in Fig. 26(b), the phases of the two waveforms are intentionally shifted for better observation.
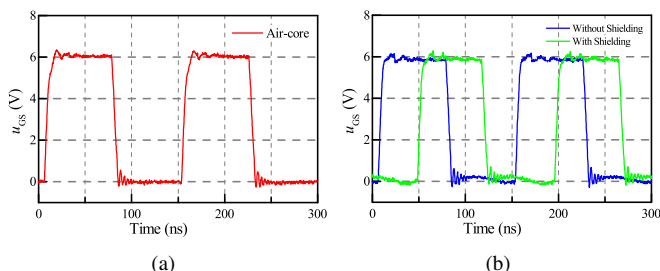

Fig. 26. Gate drive waveforms. (a) Air-core inductor. (b) Edge Inductor with / without shielding.

VII. CONCLUSION

This paper proposes a novel receiving-side design concept to compress the variation of the reflected reactance in MHz WPT systems based on the input impedance analysis of Class E family of rectifiers. This design concept guarantees the ZVS operations and stable output voltage over a wide range of load, but without the need of addition hardware. The two design parameters of the receiving side are efficiently determined

through the observation and optimization of the positions of "reactance window" to achieve the best reflected reactance compression and meet maximum output power requirement. The effective reactance compression enables straightforward application of the exiting designs using modified Class E PA and classical LCC transformation network. In addition, thanks to the simplicity of the enabled PA and compensation designs, the edge inductor becomes worthy to replace the bulky air-core finite inductance in the modified Class E PA, which further improves the compactness, especially in the height. The experimental results well validated the improved performance and compactness via the proposed receiving-side design concept and edge inductor over 5–50 Ω load range.

APPENDIX

Each Class-E-family rectifier has its different expressions of R_{eq} and C_{eq}. Here, the full-wave Class E rectifier is taken as an example.

$$R_{\text{eq}} = \frac{-(a-c)^2 - (b+d)^2 2C_{\text{r}}\pi\omega}{2C_{\text{r}}\pi\omega(a-c)} \tag{22}$$

$$C_{\text{eq}} = \frac{2C_{\text{r}}\pi(b+d)}{(a-c)^2 - (b+d)^2 2C_{\text{r}}\pi\omega} \tag{23}$$

in which a, b, c, d are

$$\begin{aligned} a &= 8(-1+D)\pi\cos(\varphi)\sin(\varphi+2\pi D) \\ b &= 4(-1+D)\pi\sin(\varphi)[1+2\sin(\varphi+2\pi D)] \\ c &= 4+\cos(2\varphi)-4\cos(2\pi D)-\cos[2(\varphi+2\pi D)] \\ d &= -\sin(\varphi)-4\sin(2\pi D)+\sin[2(\varphi+2\pi D)]. \end{aligned} \tag{24}$$

The shunt capacitor C_{r} and dc load R_{L} jointly determine the duty cycle D and phase φ.

$$C_{\text{r}} = \frac{1}{\omega R_{\text{L}}}\left[\frac{1}{4\pi} - \frac{\pi}{2}(1-D)^2 + \frac{2\pi(1-D)\cos(\varphi+2\pi D) - \sin\varphi}{4\pi\sin(\varphi+2\pi D)}\right] \tag{25}$$

$$\tan\varphi = -\frac{\pi(1-D)\sin(2\pi D) + \sin^2(\pi D)}{\pi(1-D)\cos(2\pi D) + \sin(\pi D)\cos(\pi D)}.$$

REFERENCES

[1] S. Y. R. Hui, W. Zhong, and C. K. Lee, "A critical review of recent progress in mid-range wireless power transfer," *IEEE Trans. Power Electron.*, vol. 29, no. 9, pp. 4500–4511, Sep. 2014.

[2] M. Pinuela, D. C. Yates, S. Lucyszyn, and P. D. Mitcheson, "Maximizing dc-to-load efficiency for inductive power transfer," *IEEE Trans. Power Electron.*, vol. 28, no. 5, pp. 2437–2447, May 2013.

[3] N. O. Sokal and A. D. Sokal, "Class E-a new class of high-efficiency tuned single-ended switching power amplifiers," *IEEE Journal of Solid-State Circuits*, vol. 10, no. 3, pp. 168–176, June 1975.

[4] M. K. Kazimierczuk and J. Jozwik, "Class-E zero-voltage-switching and zero-current-switching rectifiers," *IEEE Trans. Circuits Syst.*, vol. 37, no. 3, pp. 436–444, Mar. 1990.

[5] A. Reatti, M. K. Kazimierczuk, and R. Redl, "Class E full-wave low dv/dt rectifier," *IEEE Trans. Circuits Syst. I, Fundam. Theory Appl.*, vol. 40, no. 2, pp. 73–85, Feb. 1993.

[6] S. Aldhaher, D. C. Yates, and P. D. Mitcheson, "Design and development of a class EF$_2$ inverter and rectifier for multimegahertz wireless power transfer systems," *IEEE Trans. Power Electron.*, vol. 31, no. 12, pp. 8138–8150, Dec. 2016.

[7] L. Roslaniec, A. S. Jurkov, A. A. Bastami, and D. J. Perreault, "Design of single-switch inverters for variable resistance/load modulation operation," *IEEE Trans. Power Electron.*, vol. 30, no. 6, pp. 3200–3214, June 2015.

[8] S. Aldhaher, D. C. Yates, and P. D. Mitcheson, "Load-independent class E/EF inverters and rectifiers for MHz-switching applications," *IEEE Trans. Power Electron.*, vol. 33, no. 10, pp. 8270–8287, Oct. 2018.

[9] M. Fu, Z. Tang, and C. Ma, "Analysis and optimized design of compensation capacitors for a megahertz WPT system using full-bridge rectifier," *IEEE Trans. Ind. Informat.*, vol. 15, no. 1, pp. 95–104, Jan. 2018.

[10] M. Liu, M. Fu, and C. Ma, "Parameter design for a 6.78-MHz wireless power transfer system based on analytical derivation of class E current-driven rectifier," *IEEE Trans. Power Electron.*, vol. 31, no. 6, pp. 4280–4291, June 2016.

[11] S. Aldhaher, P. C. Luk, and J. F. Whidborne, "Tuning class E inverters applied in inductive links using saturable reactors," *IEEE Trans. Power Electron.*, vol. 29, no. 6, pp. 2969–2978, June 2014.

[12] Y. Lim, H. Tang, S. Lim, and J. Park, "An adaptive impedance-matching network based on a novel capacitor matrix for wireless power transfer," *IEEE Trans. Power Electron.*, vol. 29, no. 8, pp. 4403–4413, Aug. 2014.

[13] J. Choi, J. Xu, R. Makhoul, and J. M. R. Davila, "Implementing an impedance compression network to compensate for misalignments in a wireless power transfer system," *IEEE Trans. Power Electron.*, vol. 34, no. 5, pp. 4173–4184, May 2019.

[14] T. Campi, S. Cruciani, F. Maradei, and M. Feliziani, "Near-field reduction in a wireless power transfer system using LCC compensation," *IEEE Trans. Electromagn. Compat.*, vol. 59, no. 2, pp. 686–694, Apr. 2017.

[15] M. K. Kazimierczuk, B. Tomescu, and A. Ivascu, "Class E resonant rectifier with a series capacitor," *IEEE Trans. Circuits Syst. I, Fundam. Theory Appl.*, vol. 41, no. 12, pp. 885–890, Dec. 1994.

[16] K. Song, Z. Li, J. Jiang, and C. Zhu, "Constant current/voltage charging operation for series–series and series–parallel compensated wireless power transfer systems employing primary-side controller," *IEEE Trans. Power Electron.*, vol. 33, no. 9, pp. 8065–8080, Sep. 2018.

[17] X. Qu, Y. Jing, H. Han, S. Wong, and C. K. Tse, "Higher order compensation for inductive-power-transfer converters with constant-voltage or constant-current output combating transformer parameter constraints," *IEEE Trans. Power Electron.*, vol. 32, no. 1, pp. 394–405, Feb. 2017.

[18] M. Liu, M. Fu, and C. Ma, "Low-harmonic-contents and high-efficiency class E full-wave current-driven rectifier for megahertz wireless power transfer systems," *IEEE Trans. Power Electron.*, vol. 32, no. 2, pp. 1198–1209, Feb. 2017.

[19] J. M. Rivas, Y. Han, O. Leitermann, A. D. Sagneri, and D. J. Perreault, "A high-frequency resonant inverter topology with low-voltage stress," *IEEE Trans. Power Electron.*, vol. 23, no. 4, pp. 1759–1771, July 2008.

[20] S. Liu, M. Liu, S. Yang, C. Ma, and X. Zhu, "A novel design methodology for high-efficiency current-mode and voltage-mode class-E power amplifiers in wireless power transfer systems," *IEEE Trans. Power Electron.*, vol. 32, no. 6, pp. 4514–4523, June 2017.

[21] S. S. Mohan, M. del Mar Hershenson, S. P. Boyd, and T. H. Lee, "Simple accurate expressions for planar spiral inductances," *IEEE J. Solid-State Circuits*, vol. 34, no. 10, pp. 1419–1424, Oct. 1999.

[22] U. Jow and M. Ghovanloo, "Design and optimization of printed spiral coils for efficient transcutaneous inductive power transmission," *IEEE Trans. Biomed. Circuits Syst.*, vol. 1, no. 3, pp. 193–202, Sep. 2007.
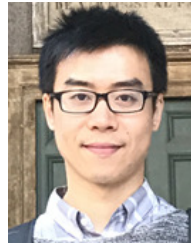
Yaoxia Shao (S'19) received the B.S. degree in mechatronic engineering from Tongji University, Shanghai, China, in 2018. He is currently working toward the Ph.D. degree in electrical and computer engineering at the University of Michigan-Shanghai Jiao Tong University Joint Institute, Shanghai Jiao Tong University, China.

His research interests include high-frequency power conversion circuits and applications in both inductive power transfer and microwave power transfer.

Ming Liu (S'15-M'17-SM'21) received the B.S. degree in mechatronic engineering from Sichuan University, Sichuan, China, in 2007, and the Ph.D. degree in electrical and computer engineering from the University of Michigan-Shanghai Jiao Tong University Joint Institute, Shanghai Jiao Tong University, Shanghai, China, in 2017.

From 2017 to 2020, he was a Postdoctoral Research Fellow with the Department of Electrical Engineering, Princeton University, USA. He joined the School of Electronic Information and Electrical Engineering, Shanghai Jiao Tong University, Shanghai, China, in 2020, where he is currently an Associate Professor of Electrical Engineering. His research interests include megahertz wireless power transfer, battery management systems, high frequency high performance power electronics for emerging applications.

Dr. Liu was the recipient of Top Ten Academic Star Award and Excellent PhD Thesis Award Nomination from Shanghai Jiao Tong University in 2016 and 2018, Research Excellence Award from AirFuel Alliance, USA, in 2019, and Best Paper Award of IEEE ECCE-Asia in 2020. He was a Guest Editor of IEEE Transactions on Industrial Informatics and serves as Chair of the Wireless Power Transfer for Energy Storage Charging Subcommittee of Energy Storage Technical Committee, IEEE Industrial Electronics Society.

Chengbin Ma (M'05-SM'18) received the B.S. degree in industrial automation from East China University of Science and Technology, Shanghai, China, in 1997, and the M.S. and Ph.D. degrees in electrical engineering from The University of Tokyo, Tokyo, Japan, in 2001 and 2004, respectively.

From 2004 to 2006, he was an R&D Researcher with the Servo Motor Laboratory, FANUC Limited, Japan. Between 2006 and 2008, he was a Postdoctoral Researcher with the Department of Mechanical and Aeronautical Engineering, University of California, Davis, USA. In 2008, he joined the University of Michigan-Shanghai Jiao Tong University Joint Institute, Shanghai Jiao Tong University, Shanghai, China, where he is currently an Associate Professor of Electrical and Computer Engineering. His research interests include battery and energy management, wireless power transfer, dynamics and motion control, and wide applications in electronic devices, electric vehicles, microgrids, smart grids, etc.

Dr. Ma was the recipient of many teaching and research awards at Shanghai Jiao Tong University, such as Teaching and Education Award in 2020 and Koguan Top Ten Research Group Award in 2014. He also received Research Excellence Award from AirFuel Alliance, USA, in 2019. He is an Associated Editor for the IEEE Transactions on Industrial Informatics and IEEE Journal of Emerging and Selected Topics in Industrial Electronics. He served as Delegate of Energy Cluster and is now Chair of Shanghai Chapter, IEEE Industrial Electronics Society.

Huan Zhang (S'19) received the B.S. degree in electrical engineering from Shandong University, Jinan, China, in 2016, and the M.S. degree in electrical engineering from Shanghai Jiao Tong University, China, in 2019. He is currently working toward the Ph.D. degree in electrical and computer engineering at the University of Michigan-Shanghai Jiao Tong University Joint Institute, Shanghai Jiao Tong University, China. He received the Best Paper Award of IEEE ECCE-Asia in 2020.

His research interests include high-frequency power electronics and its applications in megahertz wireless power transfer and energy routers. He is a Student Member of the IEEE.